A Bayesian Analysis of Class II M-type SEDs in Cha I

Jonathan Tottle[1], **Subhanjoy Mohanty**[1], **Daniel J. Mortlock**[1]

[1] *Imperial College London, Blackett Laboratory, Prince Consort Rd, London SW7 2BB, UK*

Abstract. The class II stage of a T Tauri star is characterised by the disappearance of the gaseous envelope and the presence of a primordial circumstellar disk. The observed shape of the infrared (IR) region of the spectral energy distribution (SED), where the dust continuum emission peaks, has strong implications for the geometry, structural evolution and physical conditions within the disk.

We model the IR SEDs (using 2-24 μm photometry) of 67 class II M-type objects in Cha I using the radiative transfer code of Whitney et al. (2003a) coupled to a Bayesian parameter estimation. We find that just over half of the objects appear to host 'standard' accretion disks, explaining the majority of class II SEDs, in which we observe both the unobscured star and the strong IR signature of its surrounding disk. Roughly a fifth of the objects appear edge-on, resulting in the short wavelength emission being suppressed by outer disk occlusion of the central object and inner disks. At least one object in our sample shows evidence for having a transitional disk with a large inner hole. The remaining objects are categorised as 'odd'-looking with highly unusual SEDs. A few of these may be explained by errors in the data, but for the majority it is most likely due to either exotic disk geometry, variability, or binary contamination.

1. Introduction

Observations of star forming regions have highlighted the diversity of disk structures found in young systems. Some objects appear to harbour large disks that flare outwards with increasing distance from the central star, whilst others seem to host much flatter disks. We also find disks that contain gaps/holes within them that may have been carved out by either forming planets, or perhaps by the interplay between stellar accretion and photoevaporation (Williams & Cieza 2011). These different disk permutations manifest themselves in contrasting spectral shapes across the mid/far-infrared (MIR/FIR), where the disk emission peaks. A flared disk, for example, will have increased MIR/FIR emission over a flatter disk, due to a larger quantity of reprocessed emission in the outer regions of the disk (Kenyon & Hartmann 1987), whereas a disk with a larger inner hole is noticeable due to the lack of emission above the stellar profile out to ∼10 μm (D'Alessio et al. 2005; Espaillat et al. 2007). The IR shape can also be used to detect systems that appear edge-on, in which the obscuration of the central star by the disk results in reduced stellar emission compared to the disk (Whitney et al. 2003b). We can model the SED of different disks, and fit these to the observations in order to derive the properties of the observed disks.

This study investigates the disk structure of 67 young objects selected from the nearby star forming region Cha I (Luhman 2004, 2007; Luhman et al. 2008; Luhman & Muench 2008), believed to be at an age of 2-3 Myr and a distance of ∼160 pc (Whittet et al. 1997). We restrict this investigation to those objects previously classified as containing disks (class II objects).

2. Sample and Models

2.1 Object Sample

Throughout this work we make use of the Cha I census provided in Luhman (2007), Luhman et al. (2008) and Luhman & Muench (2008). Initially we selected 94 objects, from those designated as class II by Luhman et al. (2008) and Luhman & Muench (2008) based on their spectral slopes. To obtain accurate estimates of their disk parameters through modelling, we removed those with three or more poor/missing measurements in their 2MASS, IRAC & MIPS(24 μm) photometric bands; we also omitted those earlier in spectral type than M0, so that our efforts were focussed on very low mass stars/brown dwarfs.

Spectral types and temperatures were taken from Luhman (2007) and Luhman & Muench (2008) and converted into masses using the Baraffe et al. (1998) and Chabrier et al. (2000) theoretical evolutionary tracks. To minimise fitting errors in the NIR region of the SED (which ought to be almost entirely stellar emission) model template spectra (see section 2.2) were selected using the spectral type-model template relation derived in Mohanty & Tottle (2014). J band extinctions were estimated for each object from their $J-H$ excess with respect to the spectral template colours from Luhman et al. (2010), and converted into other bands using the extinction law from Flaherty et al. (2007). As the spectral type-model template relation is already calibrated to the model spectral template NIR colours (see Mohanty & Tottle 2014 for details), we should expect almost no error in the J and H bands in our fits; this allows us to perform an accurate statistical analysis on fitting the observed disk photometry.

Composite radii, and hence luminosities, were derived for each object using a synthetic bolometric correction, found by scaling the observed J band flux to the template spectra J band flux and assuming a distance modulus of 6.05 to Cha I (Luhman 2007) according to

$$R_\star = D\left(\frac{F_{J,obs}}{F_{J,template}}\right)^{0.5}\left(\frac{T_{template}}{T_\star}\right)^2. \tag{1}$$

The stellar temperature for each object is taken from Luhman (2007) and Luhman & Muench (2008), whilst the final term on the right corrects for the disparity between the temperature of our objects and their spectral templates (see below). From this, we can calculate the stellar luminosities (using $L_\star = 4\pi R_\star^2\sigma T_\star^4$).

2.2 Model Template Spectra

In Mohanty & Tottle (2014) we derived a relation between observed spectral type and model stellar template, accurate to $\pm 25K$ for each 0.25 subclass across the M types. The best fitting template spectra for the majority of our spectral types were found to be AMES-DUSTY spectra (Allard et al. 2001), whereas a few subclasses in the mid-M region and the very late-M region were best fit by BT-Settl (Allard et al. 2012). As this relation was derived purely by comparing the shape of the IR SED in young objects across the spectral range investigated in this analysis, there could exist some disparities between the model spectral template temperatures and the spectral types temperatures (taken from the relation in Luhman et al. 2003); to account for this we scale the templates by a factor of $(T_\star/T_{template})^4$.

2.3 Radiative Transfer Code

In this study we make use of the radiative transfer code from Whitney et al. (2003a). This code uses a Monte Carlo radiative transfer structure that emits photon packets from the central protostar, and follows them through the system as they are either absorbed/re-emitted or scattered by the surrounding circumstellar disk/envelope material. The code is highly parameterised, with inputs that describe the properties of the central star, disk, and envelope, as well as properties external to the system, such as the system inclination relative to the observer.

Instead of simply fitting by eye to gain estimates of the disk properties, we opted to perform a statistical analysis; this provides more accurate estimates and has the added benefit of generating posterior distributions for each parameter. We obtain samples from the posterior distribution in the source parameters using Markov chain Monte Carlo (MCMC) techniques, specifically the Metropolis-Hastings algorithm. As we are interested in likelihood ratios for this analysis, we need to calculate the χ^2 (which is proportional to the log of the likelihood) for each model run[1]:

$$\chi^2 = \sum_{i\ \in\ \text{bands}} \left(\frac{F_{model,i} - F_{obs,i}}{\sqrt{\sigma^2_{model,i} + \sigma^2_{obs,i}}} \right)^2 \tag{2}$$

After the first run (with some initial set of parameters) is performed, the parameters are tweaked simultaneously by adding a different normal random number to each, with a mean of zero and variance set by the jump size (see Table 1). The χ^2 of this new set of parameters, χ^2_n, is compared to the previous, χ^2_o, as the new set of parameters are accepted with probability $\min\{1, \exp[\frac{1}{2}(\chi^2_n - \chi^2_o)]\}$ (Gregory 2010). The power of Metropolis-Hastings MCMC lies in the fact that even if the new set of parameters produces a worse fit, there is still a chance that

[1]We convert the output model SED into 2MASS and Spitzer photometry using the filter bandpasses & zeropoint magnitudes provided in Cohen et al. (2003) and the NASA/IPAC Infrared Science Archive: http://irsa.ipac.caltech.edu/data/SPITZER/docs/irac/calibrationfiles/spectralresponse/ and http://irsa.ipac.caltech.edu/data/SPITZER/docs/mips/calibrationfiles/spectralresponse/, as well as the spectrum of Vega (Bohlin 2007). Errors in the model photometry were calculated using the *efluxerr.dat* files output from the code.

it may be accepted as the next step in the chain (with an increasing chance the closer the new fit is to the previous fit). This is an effective way of ensuring the chain does not get stuck in any local minimum, and allows the code to efficiently find the best fitting parameter region. We impose a burn-in on our chains as the initial parameter values may not be reasonable draws from the posterior distribution; we do this by ensuring the first point in our chain passes the criterion $\chi^2 = \chi^2_{min} + 2\ln(0.1)$. This removes the beginning section of our chains in which the χ^2 is rapidly dropping as the parameters converge on their optimum values. To further strengthen our results, we also run multiple chains for each object to ensure all chains converge to the same minimum.

Table .1: Fit Parameters

Parameter	Permitted Range	Jump Size
Flaring parameter (β)	$0.5 - 1.5$	0.01
Scale height (h_0)	$0 - 0.05$	0.0006
System inclination (i)	$0 - 90$	3
Luminosity shift (L_{scale})	$0.8 - 1.2$	0.005

Table 1 lists the parameters we vary in order to fit the disk model to the data. We attempted to keep the number of free parameters as low as possible, changing those we expect to differ from object to object, so that we don't saturate the code with too many variables. The flaring parameter and scale height are simultaneously defined by the equation $h = h_0(\varpi/R_\star)^\beta$, where ϖ is the radial coordinate in the disk midplane, and h_0 is defined as the scale height (in units of $R_\star$). We also use a variable luminosity shift, or a 'scaling', of the output SED, allowing us to obtain the best possible fit whilst accounting for small uncertainties in object temperatures, radii and distances. The system inclination is defined as 0° when the disk is face-on to our line of sight, and 90° for edge-on.

Table .2: Fixed Parameters

Parameter	Fixed Value
$L_\star/R_\star/M_\star$	see Section 2.1
Number of photons (N_γ)	4×10^6
$\dot{M}$	from F_{H_α}
M_{disk}	$M_\star/100$
R_{in}	R_{sub}
R_{out}	100AU
disk density parameter (α)	$\beta + 1$
envelope density (ρ_{amb})	0

Table 2 lists the important parameters which we have decided to fix for our model runs. The number of photons, which acts not as a physical property but purely as a numerical precision parameter in the code, was chosen to be 4×10^6 as a compromise between computational time and model photometric errors. Accretion rates (necessary for computing the contribution of accretion luminosity to the output SED) were calculated for our objects using their Hα fluxes when available (Luhman 2004), which were converted into $\dot{M}$ using the relation in Herczeg & Hillenbrand (2008). When no Hα information was available we instead used the $\dot{M} \propto M_\star^2$ relation from Mohanty et al. (2005) to estimate accretion rates. The disk density parameter α (defined in $\rho \propto r^{-\alpha}$) was set as $\beta+1$, equivalent to setting the surface density exponent equal to -1 (i.e., $\Sigma \propto r^{-1}$), so to agree with observations (Andrews et al. 2010). We decided to ignore all envelope properties by setting the envelope material density to zero, so as to concentrate our analysis solely on the disk structure.

3. Analysis

Of the 67 objects in our sample we were initially able to accurately model 31, just under half our sample. For the others, we found that the MCMC acceptance ratios (the fraction of accepted new parameter sets over the total number of iterations) were so low that we were unable to draw any reasonable conclusions from their results. We were able to split these poorly-fit objects into two categories: those which gave evidence for being edge-on; and those which simply looked 'odd'.

3.1 Well-fit Objects

For the well-fit objects we were able to find good estimates of their disk properties as well as confidence intervals on these derived parameters, based on the standard deviation of their posterior distributions. The distributions from the MCMC analysis for object 2M J110854-763241 are shown in Figure 1, highlighting the correlations between each parameter, as well as their posterior distributions. For this object we also show the best fitting model SED in Figure 2, which emphasises how good the fits that we can derive from an MCMC process are; for this fit in particular we find a χ^2 of just 1.65. In Tottle et al. (2014) we will attempt to investigate the derived parameter results for the sample as a whole, as well as search for correlations between the disk and stellar properties.

3.2 Edge-on Objects

Of the poorly-fit objects, we were able to identify 13 as edge-on candidates. Extinctions were previously derived for all of the objects in the sample in Luhman (2007) and Luhman & Muench (2008), using the colour excess in their optical spectra. Unlike the NIR shape, which is heavily altered by absorption in an edge-on disk, the optical shape should be roughly retained as we observe it purely in scattered light. In contrast, for objects that do not appear edge-on it is usual to find an agreement between optically & NIR-derived extinctions, as the overall shape of each remains unaffected as the light travels to Earth. It is therefore possible to identify edge-on candidates by finding drastically different estimates of extinction from optical/NIR colour excesses, which is true for 11 of our poorly-fit objects. A further two objects were classified as edge-on candidates due to their extremely subluminous appearance, with both of them differing in luminosity by roughly two orders of magnitude from what one might expect whilst retaining a more usual disk profile (as expected for almost completely edge-on objects (Whitney et al. 2003b)).

For these objects we re-calculate their IR photometry using their optical extinctions (which we believe to be a more accurate estimation), and attribute luminosities based on

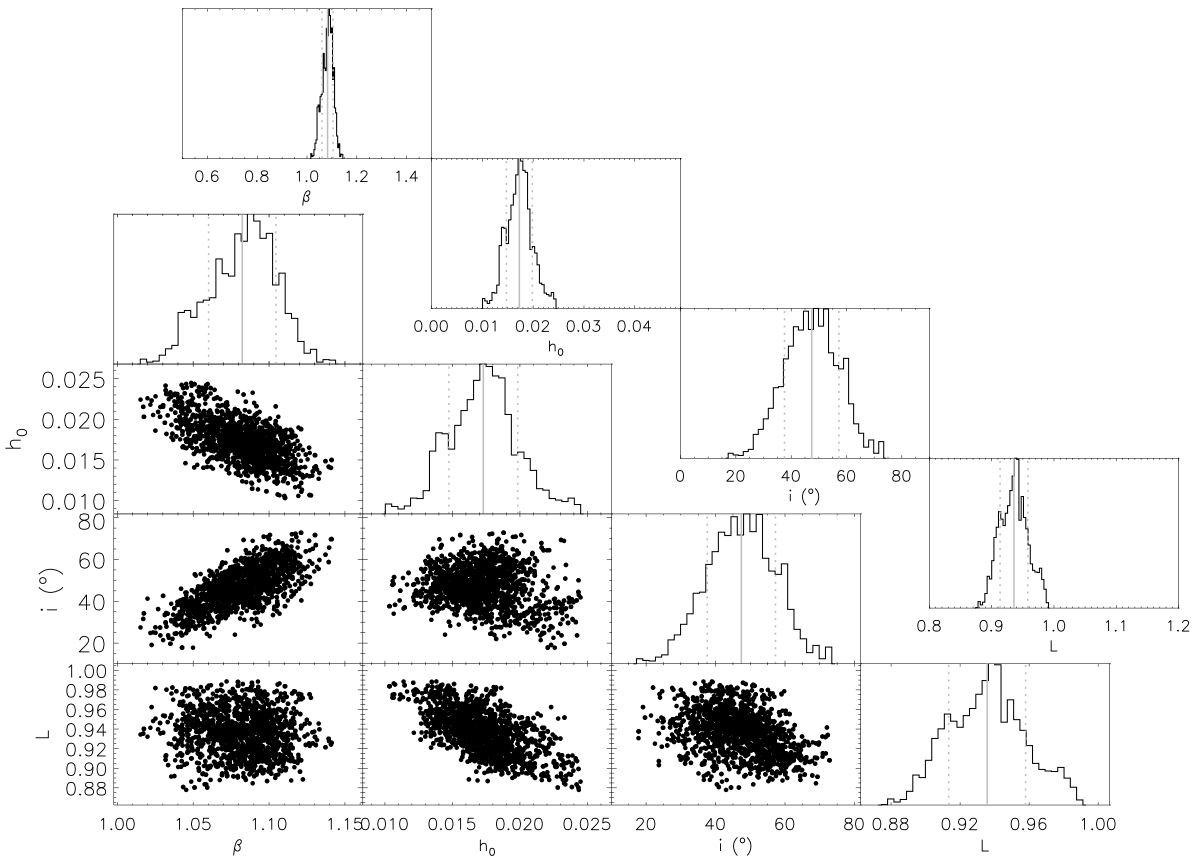

Figure .1: 2-D scatter plots and 1-D histograms of the MCMC chains (after burn-in removal) for object 2M J110854-763241. The scatter plots highlight the correlations between each of the 4 fit parameters in the model, e.g., in this case we can see there exists a correlation between β and i. The histograms show the posterior distributions for each parameter; we also include the mean (solid grey line) and standard deviation (dotted grey lines) values. In the top right we present these posterior distributions across the entire allowed parameter range, highlighting how well constrained each parameter is in the expected range.

the Baraffe et al. (1998) and Chabrier et al. (2000) theoretical evolutionary tracks, since any bolometric correction will be subject to a diminished J band. We show examples of these objects in Figure 3, including the two subluminous objects Cha J110819-773152 and 2M J111110-764157. In the others, we observe increased emission from J through to K_s due to the disk material absorbing a larger quantity of the short-wavelength emission, which is both the source of the discrepancy in the NIR/optically-derived extinctions, and the reason for the poor model fits to the data. We are currently in the process of attempting to model these objects using a modified version of our code.

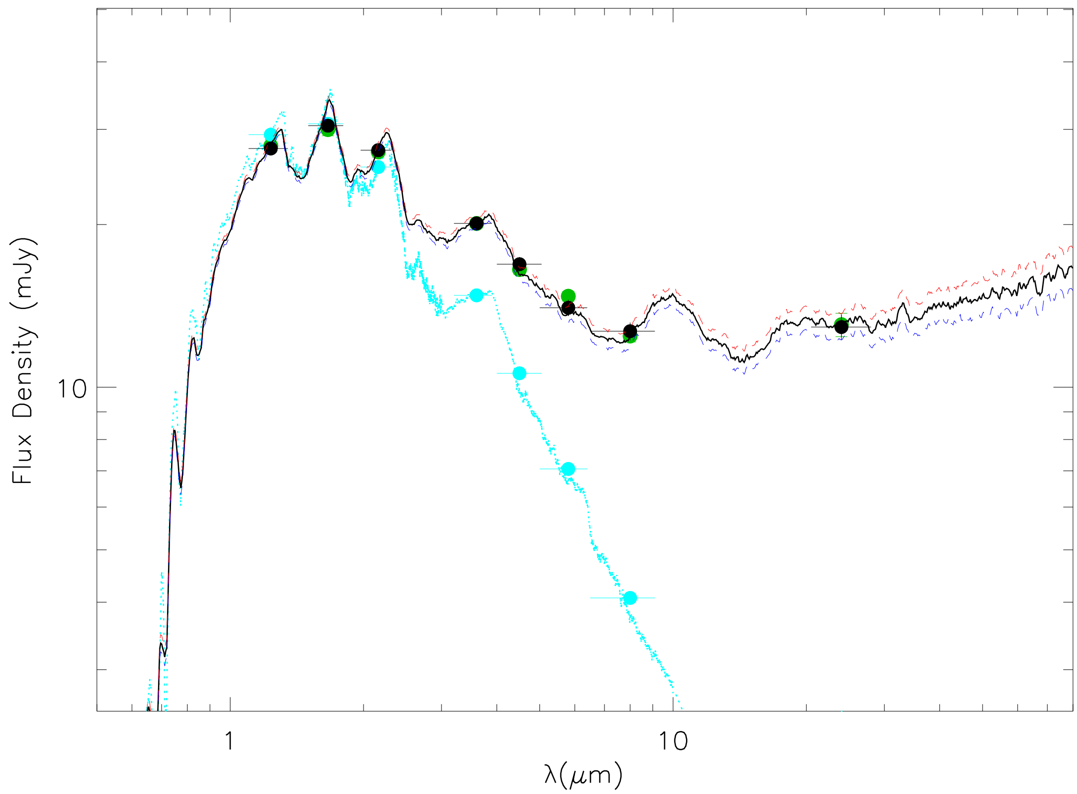

Figure .2: Best fit model (black line/data points) with errors (red/blue dashed lines) compared to the observed photometry (green data points) for object 2M J110854-763241. For the most part, the model photometric values are almost identical to the observed values, and error bars are too small to be seen. The stellar template is also shown (turquoise line/data points) underneath.

3.3 'Odd' Objects

The remaining poorly-fit objects were examined in an attempt to find the cause of error in the model fitting. We believe we have solved the issue for five of these objects, out of a total of 23, under certain assumptions. One of them, 2M J110713-774349, gave clear evidence of containing a large inner hole, and a good fit to the data was found when modelling a disk with an inner hole radius of ∼6 AU. We show the best-fitting model for this object in Figure 4. The inner hole is immediately apparent from the lack of disk emission out to at least 8 μm.

When available, we combined multi-epoch IRAC & MIPS photometry to minimise observational errors; however, this can lead to skewed photometry stemming from MIR variability. This certainly seems to be the case for 2M J110716-773553, which was fit well with a standard disk model when using photometry taken on a single date. A further three objects each

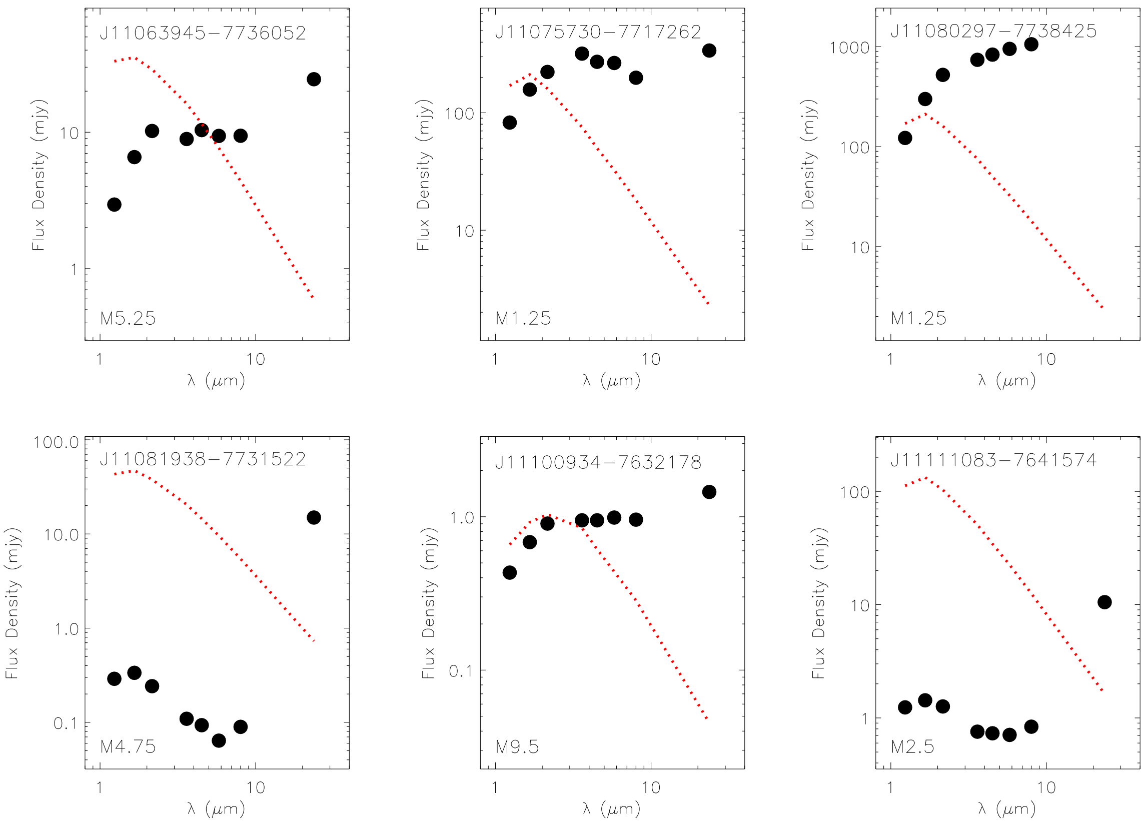

Figure .3: IR photometry for the 6 of the 13 suspected edge-on objects in our sample, with each object's respective model stellar template (red dashed line) shown for comparison. The observed NIR shapes are clearly different than the templates, whilst the observed J-band emission appears dimmer throughout due to absorption in the occulting disk. Object names and spectral types are given on each plot.

had an overly bright 8 μm band that could not be fit with any model, yet showed no signs of variability; however, we were able to obtain excellent model fits when masking out their 8 μm values. An example of one of these objects in shown in Figure 5. Clearly, an almost perfect fit to the data is found when ignoring the 8 μm observation; when excluding it the χ^2 value is just 0.48 (putting it among the best fits in our sample), compared to $\chi^2 = 17.04$ when including it. It is currently unknown what could cause such spuriously high 8 μm measurements, but one possibility is reduced turbulence in the disk causing PAH emission to rise above the expected continuum (Dullemond et al. 2007).

The remaining objects do not seem to have any obvious reasons why they are strange, but could be due to errors in the data, binary contamination, or exotic disk geometry. We are currently investigating these objects in further detail.

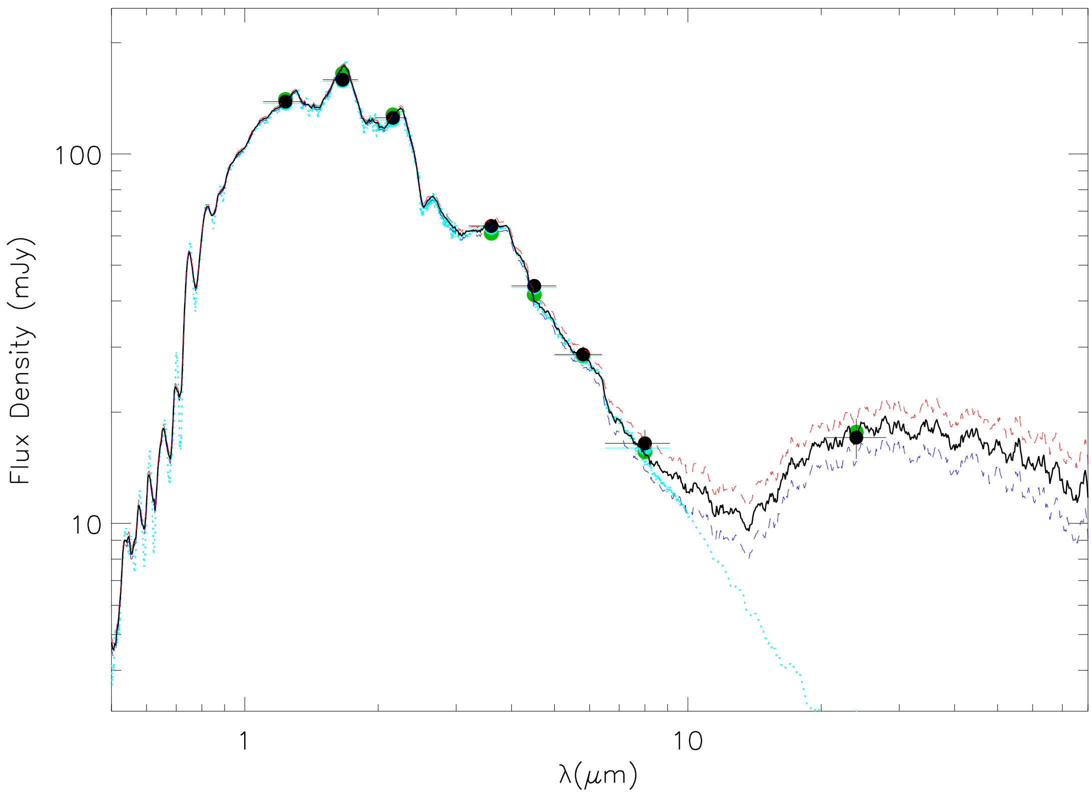

Figure .4: Same as Figure 2 for object 2M J110713-774249. Fit with a disk model of inner hole size 5.84AU, the SED shows the observed emission following the model stellar template (turquoise) out to ∼10 μm, after which point the emission from the (cooler) outer disk dominates.

4. Discussion

We have modelled the SEDs of 67 class II M-type objects in Cha I across the IR, utilising both the radiative transfer code of Whitney et al. (2003a) and a Bayesian approach. 31 of our 67 objects were able to be fit with a standard disk model; upon further investigation we managed to obtain fits to another five, through either masking out spurious photometry, identifying variability, or fitting with an inner hole model. This means we have been able to obtain reliable estimates of the disk parameters for over half our sample. A further 13 objects have been identified as most likely being edge on, and are currently in the process of being fit with a modified version of the code. Finally, we have 18 objects remaining whose SED shape we have not successfully fit for reasons unknown, possibly due to errors in the data, binary contamination, or exotic disk geometry. We are hopeful that further analysis will reveal the explanation for these 'odd' SEDs.

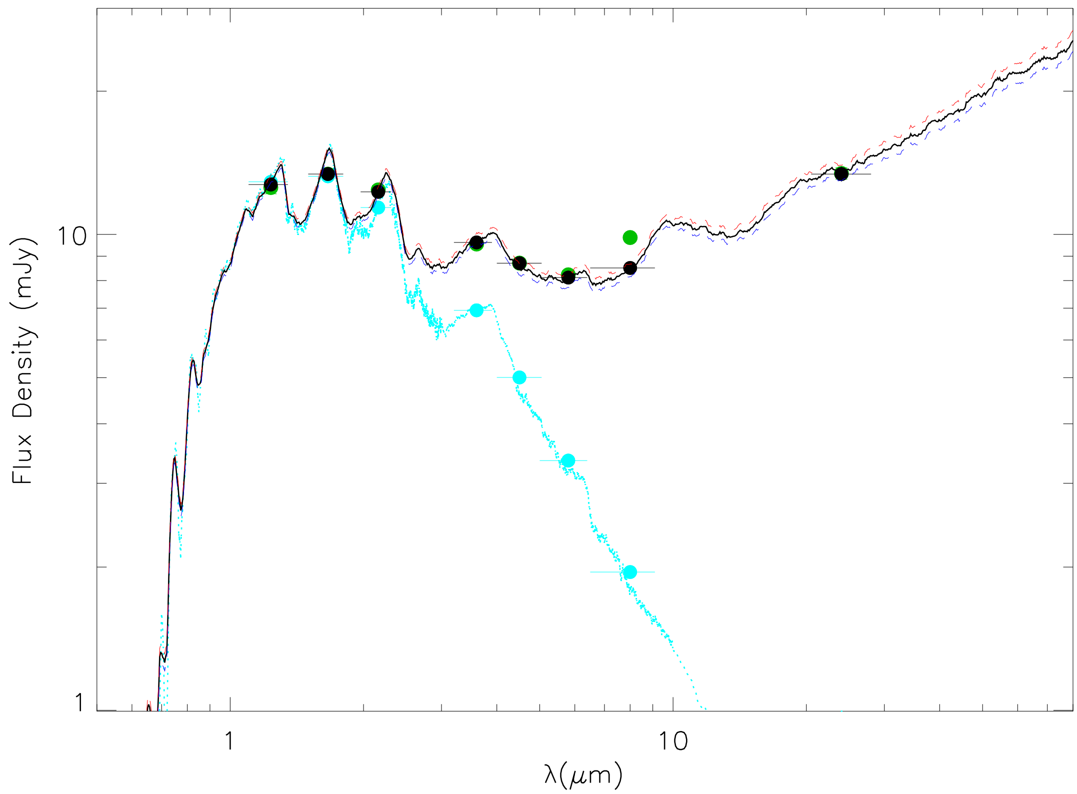

Figure .5: Same as Figure 2 for object 2M J111041-772048. This best fit model was found by masking out the 8 μm in the χ^2 evaluation.

Acknowledgements. Many thanks to Barbara Whitney and Kevin Luhman for their correspondence regarding this work. Jonathan Tottle would also like to acknowledge the Royal Astronomical Society grant scheme for support with attending Cool Stars 18.

References

Allard, F., Hauschildt, P. H., Alexander, D. R., et al., 2001, ApJ, 556, 357

Allard, F., Homeier, D., Freytag, B., Sharp, C. M., 2012, EAS, 57, 3

Andrews, S., Czekala, I., Wilner, D. J., et al., 2010, ApJ, 710, 462

Baraffe, I., Chabrier, G., Allard, F., Hauschildt, P. H., 1998, A&A, 337, 403

Bohlin, R. C., 2007, ASP conf. series, 364

Chabrier, G., Baraffe, I., Allard, F., Hauschildt, P. H., 2000, ApJ, 542, 464

Cohen, M., Wheaton, Wm. A., Megeath, S. T., 2003, AJ, 126, 1090

Dullemond, C. P., Henning, Th., Visser, R., et al. 2007, A&A, 473, 457

D'Alessio, P., Hartmann, L., Calvet, N., et al., 2005, ApJ, 621, 461

Espaillat, C., Calvet, N., D'Alessio, P., et al., 2007, ApJ, 664, L111

Flaherty K. M., Pipher, J. L., Megeath, S. T., et al., 2007 ApJ, 663, 1069

Gregory, P., 2010, *Bayesian logical data analysis in the physical sciences*, Cambridge: Cambridge University Press

Herczeg, G. J., Hillenbrand, L, A., 2008, ApJ, 681, 594

Kenyon, S. J., Hartmann, L., 1987, ApJ, 323, 714

Luhman, K. L., Stauffer, J. R., Muench, A. A., et al. 2003, ApJ, 593, 1093

Luhman, K. L. 2004, ApJ, 602, 816

Luhman, K. L. 2007, ApJS, 173, 104

Luhman, K. L., Allen, L. E., Allen, P. R., et al., 2008, ApJ, 675, 1375

Luhman, K. L., Muench, A. A., 2008, ApJ, 684, 654

Luhman, K. L., Allen, P. R., Espaillat, C., et al., 2010, ApJS, 186, 111

Mohanty, S., Jayawardhana, R., Basri, G., 2005, ApJ, 626, 498

Mohanty, S., Tottle, J., 2014, in prep.

Tottle, J., Mohanty, S., Mortlock, D. J., 2014, in prep.

Whitney, B. A., Wood, H., Bjorkman, J. E., Wolff, M. J., ApJ, 591, 1049

Whitney, B. A., Wood, H., Bjorkman, J. E., Cohen, M., ApJ, 598, 1079

Whittet, D. C. B., Prusti, T., Franco, G. A. P., et al., 1997, A&A, 327, 1194

Williams, J. P., Cieza, L. A., et al., 2011, ARAA, 49, 67

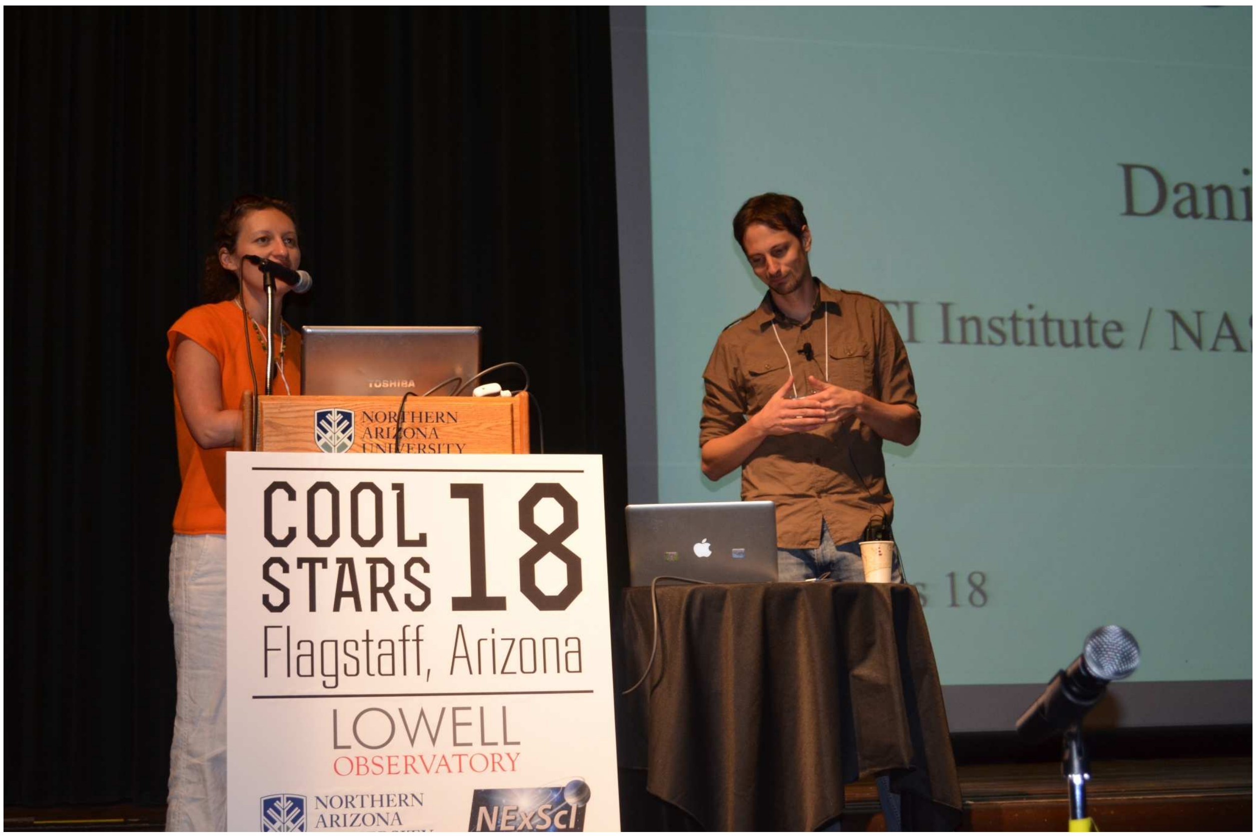

Evgenya Shkolnik introduces Daniel Huber for his asteroseismology talk.